RESEARCH ARTICLE

EcoMat
FUNCTIONAL MATERIALS FOR GREEN ENERGY AND ENVIRONMENT

WILEY

N-stabilized metal single atoms enabled rich defects for noble-metal alloy toward superior water reduction

Haiyan Jin[1] | Lok Wing Wong[1] | Ka Hei Lai[1] | Xiaodong Zheng[1] |
Shu Ping Lau[1] | Qingming Deng[2] | Jiong Zhao[1,3] (ID)

[1]Department of Applied Physics, The Hong Kong Polytechnic University, Kowloon, Hong Kong, China

[2]Physics Department and Jiangsu Key Laboratory for Chemistry of Low-Dimensional Materials, Huaiyin Normal University, Huaian, China

[3]Polytechnic University of Hong Kong Shenzhen Research Institute, Shenzhen, China

Correspondence
Shu Ping Lau, Department of Applied Physics, The Hong Kong Polytechnic University, Kowloon, Hong Kong, China.
Email: apsplau@polyu.edu.hk;

Qingming Deng, Physics Department and Jiangsu Key Laboratory for Chemistry of Low-Dimensional Materials, Huaiyin Normal University, Huaian, China.
Email: qingmingdeng@gmail.com;

Jiong Zhao, Department of Applied Physics, The Hong Kong Polytechnic University, Kowloon, Hong Kong, China.
Email: jiongzhao@polyu.edu.hk

Abstract

The traditional methods of introducing defects into alloy catalysts, such as dealloying, quenching, and doping, usually require complicated processes, rendering less controllability to the products and performances. Herein, a simple fabrication method for vacancy-rich IrCo alloy nanoparticles supported on N-doped carbon sheets (denoted as D-IrCo/NC) is applied by post-annealing the single atom (Ir and Co) dispersed precursors. The mobile single atoms and the coalescences of metallic clusters are directly observed via in situ transmission electron microscopy. Compared to the alloy catalysts obtained by direct calcination or other traditional methods, the D-IrCo$_{4.9}$/NC catalyst is enriched with vacancy defects and only demands an overpotential of 14 mV at $j = 10$ mA/cm^2 for HER. Density functional theory (DFT) calculations reveal that the under-coordinated Ir sites possess the lowest hydrogen adsorption energy. This novel preparation method is universal, and this work also provides a facile strategy to fabricate highly defective alloy catalysts evolved from single atom precursors.

KEYWORDS

alloy, defects, hydrogen evolution, in situ TEM, single atoms, vacancies

1 | INTRODUCTION

In terms of solving global warming and energy crisis, hydrogen has been recognized as a clean, zero-carbon emission and renewable alternative for fossil fuel-based resources.[1–4] Hydrogen production from electrocatalytic water splitting has attracted great attention due to its high efficiency, high purity, stable output, and eco-friendliness. Noble metal-based catalysts are currently deemed the best candidates for hydrogen evolution reaction (HER) in virtue of their high catalytic efficiency, fast kinetics, and robust operation.[5–8] Meanwhile, a variety of strategies have been invented to reduce the high cost and maximize the catalytic efficiency of noble metal catalysts. Among them, alloying with low-cost transition metals is a popular method that can modulate the electronic density of states near Fermi level of noble metals and the adsorption energies of intermediates, thus boosting the intrinsic activity.[9–11] Besides, the synergistic effect between the transition metal and noble metal can remarkably improve the catalytic performance.[12]

Despite the introduction of defects into alloys hosting rearranged atoms and redistributed charges is a desirable strategy to engineer the electronic structures of metal atoms,[13–18] the conventional synthesis routes for alloy catalysts, including the reduction of metal salts in organic solvents,[19] the aqueous wet-chemical method[20,21] and electrodeposition[22] are difficult to achieve high yield and good control on the atomic defects in catalysts. Additionally, the common methods for defect generation, including dealloying,[23] quenching,[24] doping,[25] etc. require complicated processes and high costs. Many recent works focus on developing single-atom catalysts from the metal bulks or clusters.[26–28] Nevertheless, the reverse transformation-from single atoms to clusters is rarely explored. Clusters composed of multiple atoms are demanded for complicated reactions involving multiple active sites,[29,30] while single atoms cannot meet the requirement. The N-coordinated single-atom catalysts, which are accessible by recent progress in electrocatalyst research,[31,32] have the potential to be the precursors of defective alloy catalysts upon thermal treatment. Such formation kinetics are controlled by the successive release of nitrogen content and single atom diffusion in the post-annealing process.

Herein, IrCo alloy nanoparticles with abundant atomic defects anchored on N-doped carbon sheet catalyst (denoted as D-IrCo/NC, D means defects) evolved from N-coordinated Ir/Co single atoms are prepared by controlling the nitrogen content under thermal treatment. We employ in situ scanning transmission electron microscopy (STEM) to study the mobile trajectories of the single-atom precursors and coalescences of metal clusters. Benefiting from the introduction of defects

(mainly vacancies) into the IrCo alloy structures by the above method, the resulting $D-IrCo_{4.9}/NC$ demonstrates extraordinary catalytic performance for HER with low overpotential (14 mV at $j = 10$ mA/cm^2), small Tafel slope (35 mV/dec) and fast charge transfer. Particularly, the mass activity of $D-IrCo_{4.9}/NC$ at an overpotential of 20 mV is 3.6 times larger than its counterpart $IrCo_{5.2}/NC$ with fewer defects (IrCo alloy clusters supported on N-doped carbon prepared by calcinating the inorganic precursors of Ir and Co at high temperature). DFT calculations reveal that the specific defects decrease the adsorption energy of hydrogen, accelerating the evolution of hydrogen. Impressively, the Ir sites at vacancies possess the highest reactive activity. This work provides new insights into electrochemistry-single atoms are not only promising electrocatalysts but also ideal precursors for defective catalyst particles. Moreover, the strategy elaborated in this work is universal for fabricating other noble metal catalysts with rich defects.

2 | EXPERIMENTAL SECTION

2.1 | The preparation of D-IrCo$_{4.9}$/NC

Glucose weighing 0.4 g, 10 g dicyandiamide, 17.16 mg K_2IrCl_6, and 50.6 mg $Co(NO_3)_2 \cdot 6H_2O$ were dissolved into 120 ml deionized water and stirred continuously at 80°C until dried. The obtained powder was finely ground and calcinated in a tube furnace. The annealing temperature was firstly risen to 600°C at a heating rate of 5°C/min and then was further increased to 800°C at 2°C/min and kept for 2 h under flowing 200 sccm argon. The acquired product was Ir and Co single-atom dispersed catalysts supported on N-doped carbon sheet (Ir_1Co_1/NC). Afterward, Ir_1Co_1/NC was annealed at 1000°C for 1 h at a heating rate of 5°C/min under an Ar atmosphere and then $D-IrCo_{4.9}/NC$ was obtained (the mass ratio of Co and Ir is 4.9). $D-IrCo_{6.5}/NC$ (the mass ratio of Co/Ir is 6.5) and $D-IrCo_{3.5}/NC$ (the mass ratio of Co/Ir is 3.5) were synthesized by applying same method to that of $D-IrCo_{4.9}/NC$ except for the mass of K_2IrCl_6 (For $D-IrCo_{6.5}/NC$, it is 10.3 mg, for $D-IrCo_{3.5}/NC$, it is 27.46 mg). The preparations of the comparative samples of Co/NC and Ir/NC were similar to $D-IrCo_{4.9}/NC$ apart from the different metal precursors. Similarly, $D-IrFe_{4.9}/NC$ and $D-RhCo_5/NC$ were also fabricated, except that the metal precursors were replaced by 75.9 mg $Fe(NO_3)_3 \cdot 9H_2O$ and 17.4 mg $RhCl_3 \cdot xH_2O$, respectively.

2.2 | Electrochemical measurements

A three-electrode glass cell was adopted for electrochemical measurements by using CHI 760E workstation. The

commercial glassy carbon electrode (GCE, 5 mm diameter, 0.196 cm^2) was utilized as the working electrode. The presented current density referred to the geometric surface area of the glassy carbon electrode. A saturated calomel electrode (SCE) and graphite rod served as the reference electrode and the counter electrode, respectively. The working electrode was prepared as described below: 500 μl ethanol, 3 mg of catalyst and 20 μl 5 wt% Nafion solutions were mixed by ultrasonic 60 min. Then, 10 μl catalyst ink suspension was coated onto the polished GC electrode and was left to dry in air. The loading mass of catalysts on GCE is 0.29 mg/cm^2. The mass activity is calculated based on the mass of metallic Ir coated on the GCE. The mass of metal Ir loaded on GCE is about 4.1 μg/cm^2 based on the below ICP-AES. The potential, measured against a SCE electrode, was converted to the potential versus the reversible hydrogen electrode (RHE) according to $E_{vsRHE} = E_{vsSCE} + E^{\theta}_{SCE} +- 0.059$ pH. Electrochemical measurements of catalysts were measured in 0.5 M H$_2$SO$_4$ solution after purging the electrolyte with N$_2$ gas for 30 min at 25°C. The linear sweep voltammograms (LSV) were performed at a scan rate of 2 mV/s. To get the stable lsv curve, the catalyst was firstly scanned for 20 cycles. The Tafel slopes were determined by fitting the linear portion of the LSV plots. For the durability test, the catalyst was scanned in a potential range of 0.02 to −0.1 V (vs RHE) for 10 000 cycles (without iR compensation). Moreover, the electrocatalytic activities of other catalysts were measured under similar conditions; and the corresponding electrocatalytic results were included in the main text. The electrochemical impedance spectroscopy (EIS) is conducted from 100 KHz to 0.01 Hz at an overpotential of 15 mV. All data have been ohmic drop corrected based on impedance spectroscopy unless otherwise specified.

2.3 | DFT simulations

Spin-polarized density function theory (DFT) calculations are performed by using the Vienna ab initio Simulation Package (VASP) program package[33,34] within the projector augmented wave (PAW)[35] to explore geometries and electronic properties of ReS$_2$. The exchange-correlation interactions are described with the generalized gradient approximation (GGA)[36] in the form of the Perdew, Burke, and Ernzernhof (PBE) functional.[37] The kinetic energy cutoff for the plane-wave basis set is chosen as 450 eV, and the distance of the vacuum layer is set to be more than 20 Å, which is sufficient to avoid interlayer interactions. The DFT-D3 scheme of Grimme for the vdW correction is applied on Ir (111) surface.[38] The pristine slab contains 108 Ir atoms. The electronic SCF tolerance is set to 10^{-5} eV. Fully relaxed geometries and lattice constant are obtained by optimizing all atomic positions until the Hellmann–Feynman forces are less than 0.02 eV/Å. The k-points samplings with a gamma-centered Monkhorst-Pack scheme[39] are $5 \times 5 \times 1$ for structural optimizations. Converting the calculated DFT adsorption energies (ΔE) into Gibbs free energies (ΔG) is taking entropic (TS) and ZPE corrections to adsorbed species into account from the previous report,[40] so that $\Delta G_H = \Delta E_H + 0.24$ eV.

3 | RESULTS AND DISCUSSION

Iridium and cobalt single-atom dispersed nitrogen-doped carbon sheets (Ir$_1$Co$_1$/NC) are firstly prepared by the reaction of D-(+) glucose, dicyandiamide, K$_2$IrCl$_6$ and Co(NO$_3$)$_2$·6H$_2$O in water and then annealed in a tube furnace at 800°C. Afterward, D-IrCo$_{4.9}$/NC with rich defects (IrCo alloy clusters anchored on N-doped carbon sheets) can be obtained by further calcinating Ir$_1$Co$_1$/NC at 1000°C as depicted in Figure 1A. The transmission electron microscopy (TEM) image of Ir$_1$Co$_1$/NC shows the morphology of nanosheets (Figure S1). High-angle annular dark-field STEM (HAADF-STEM) image of Figure 1B reveals that abundant Ir and Co single atoms (white spots) are distributed on nitrogen-doped carbon sheet. The N content in Ir$_1$Co$_1$/NC is 23.4 wt% based on elemental analysis in Table S1, and Ir and Co single atoms are stabilized by four neighboring nitrogen (MN$_4$) based on the previous report. Large amounts of nanoclusters generate with the rapidly decreased N content (1.5 wt%) in D-IrCo$_{4.9}$/NC, and the average size is 3.76 nm, as observed in Figure 1C and Figure S2a–c. For Co/NC without Ir, the clusters (23 nm) become much larger during annealing as shown in Figure S3a,b. The metal contents of Ir and Co in D-IrCo$_5$/NC are 1.4 and 6.9 wt% according to the ICP-AES, as shown in Table S1, respectively. It is demonstrated that Co, Ir, C, N, and O are evenly distributed on the nanosheet of D-IrCo$_{4.9}$/NC based on the EDS mappings in Figure S4. The EDS line scan on individual clusters in Figure S5 indicates that Co and Ir are uniformly dispersed in nanoparticles. In the overlay mapping of Figure S4d, the Co element occupies a large proportion for large clusters while small clusters contain more Ir atoms. Specifically, the atomic ratio of Ir/Co for the cluster with a size smaller than 4 nm is greater than one, and the value is smaller than one for nanoparticles over 4 nm, as analyzed in Figure S6 and Table S2. To compare with the structure of D-IrCo$_{4.9}$/NC derived from single atom precursors, IrCo$_{4.9}$/NC (IrCo alloy supported on N-doped carbon) is prepared by the traditional impregnation and calcination method, that is,
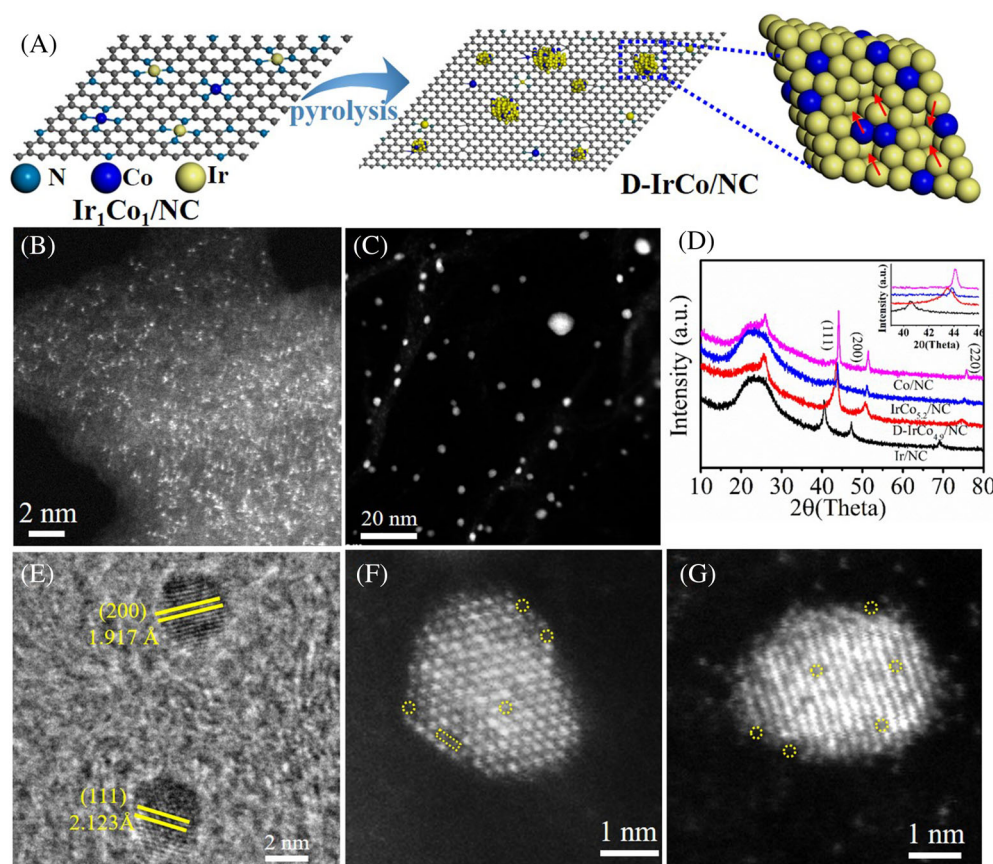
FIGURE 1 (A) Schematic illustration of the preparation process of D-IrCo/NC (atom vacancies pointed by red arrow), HAADF-STEM image of (B) Ir_1Co_1/NC and (C) D-IrCo$_{4.9}$/NC, (D) XRD patterns of catalysts, (E) HRTEM image of D-IrCo$_{4.9}$/NC, (F,G) Atomic HAADF-STEM images of individual cluster from D-IrCo$_{4.9}$/NC, showing the existence of multiple vacancies (marked by yellow circular and rectangular dotted lines)

annealing the inorganic precursors of Ir and Co and NC at high temperature as described in the Supporting Information. As shown in the X-ray diffraction (XRD) pattern of Figure 1D, the diffraction peak indexed to (111) plane of D-IrCo$_{4.9}$/NC at 43.5° is located between metallic cobalt (44.1°) and iridium (40.6°) and the lattice planes of (200) and (220) for D-IrCo$_{4.9}$/NC in Figure 1D also demonstrate similar properties, indicating the formation of IrCo alloy. Moreover, in Figure S2d, with the increased Ir content, the peaks of (111), (200), and (220) planes for D-IrCo$_{6.5}$/NC, D-IrCo$_{4.9}$/NC, and D-IrCo$_{3.5}$/NC gradually shift to negative positions, closer to those of metallic Ir, again confirming the formation of IrCo alloy. In the HRTEM image of D-IrCo$_{4.9}$/NC in Figure 1E, the lattice fringe distances of 2.123 Å and 2.076 Å in Figure S2e should be assigned to the (111) plane of IrCo alloy, and these values are between metallic Co (2.047 Å) and Ir (2.217 Å). Similarly, the lattice spacing of 1.917 Å in Figure 1E is ascribed to the (200) plane of IrCo alloy. It is noteworthy that the large cluster is surrounded by several graphitic carbon layers in Figure S2e, which is beneficial to improve the HER stability. The electronic interaction between Ir and Co can be reflected by the X-ray photoelectron spectroscopies (XPS) of catalysts. As observed in Figure S7, the peak position of Ir 4f in D-IrCo$_{4.9}$/NC and IrCo$_{5.2}$/NC shifts negatively relative to Ir/NC, indicating

the electron transfer from Co to Ir. Correspondingly, the binding energies of Co 2p in D-IrCo$_{4.9}$/NC and IrCo$_{5.2}$/NC increase in comparison with that in Co–NC, again verifying that some electrons from Co of IrCo alloy transfer to Ir, which is beneficial to enhancing the HER activity. The atomic HAADF-STEM images of an individual cluster from D-IrCo$_{4.9}$/NC in Figure 1F, G and Figure S8 suggest abundant Ir/Co vacancies generated as marked by the yellow circular and rectangular dotted lines. Furthermore, the rough surfaces of clusters also reveal the formation of vacancies. It is because some Ir or Co atoms detach from the peripheral nitrogen atoms, forming clusters, while some still exist in the form of single atoms (vacancies in the cluster), which is in accordance with the rapidly reduced nitrogen content from Ir_1Co_1/NC (800°C) to D-IrCo$_{4.9}$/NC (1000°C). In contrast, the surfaces of IrCo$_{4.9}$/NC nanoparticles prepared by the traditional method are smooth, and fewer vacancies exist, which manifests the crucial role of single atoms in promoting vacancies. To further investigate the coordination structure of catalysts, X-ray absorption fine structure (XAFS) spectroscopy is performed. As shown in Figure S9 and Tables S3 and S4, the coordination number of Co—Co/Ir bond ($CN_{Co—Co/Ir}$) in D-IrCo$_{4.9}$/NC is close to 9, which is lower than that in IrCo$_{5.2}$/NC ($CN_{Co—Co/Ir}$ = 11) from Co K-edge, suggesting more

FIGURE 2 The direct observation of (A–H) the mobility of highly-density dispersed single atom to form a cluster for Ir_1Co_1/NC (two series from A–D and E–H, respectively) and (I–L) the coalescences of two metal clusters from $D-IrCo_{4.9}/NC$ by in situ scanning transmission electron microscopy (STEM); (A–H) scale bar = 1 nm, (I–L) scale bar = 2 nm
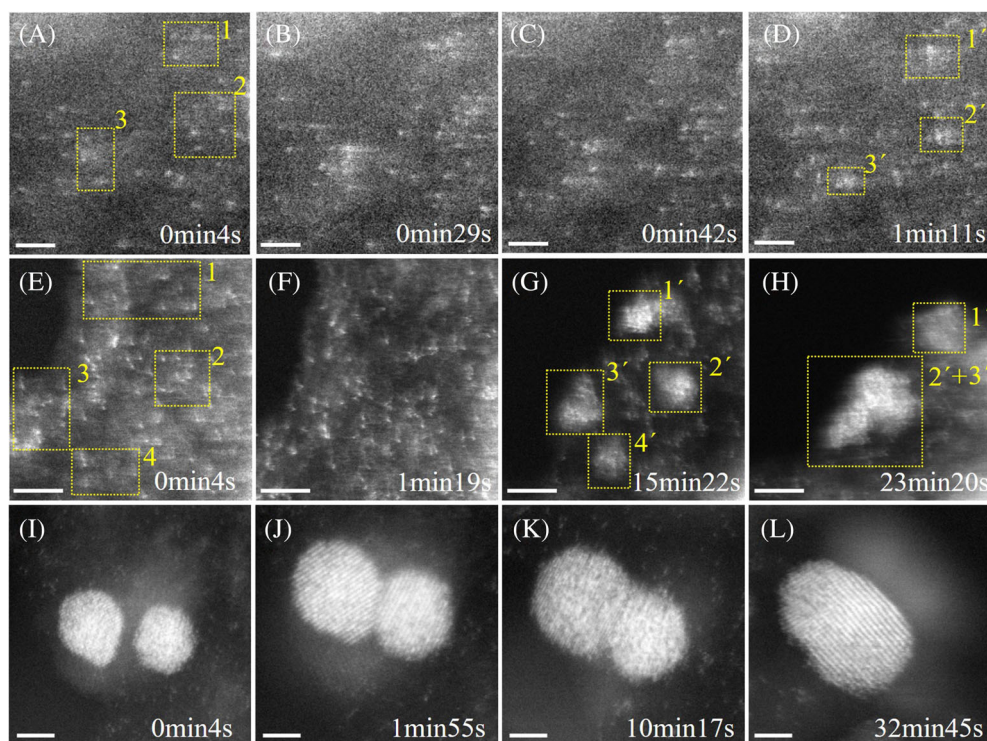
vacancies exist in $D-IrCo_{4.9}/NC$. Similarly, for Ir L_3-edge, the $CN_{Ir–Co/Ir}$ of $D-IrCo_{4.9}/NC$ (7.8) is smaller than that of $IrCo_{5.2}/NC$ (9.9).

To further clarify the formation process of IrCo alloy from Ir/Co single-atom dispersed precursors, the in situ scanning transmission electron microscopy (STEM) is performed.[41] The continuous irradiation of a high-energy electron beam is applied to simulate the sintering process of single-atom catalysts under high temperature. As shown in Figure 2A–H, small clusters of 1 nm size evolve from single atoms with the increased irradiation time of the electron beam. Ultrasmall clusters composed of tens of atoms appear as marked in Figure 2D,G,H, while on the same area of Figure 2A,E, only isolated single atoms or sub-nanometer clusters with fully exposed atoms exist.[42] Therefore, the formation of clusters is promoted by the migration and collision of single atoms under high energy. It is also concluded in Figure 2A–H that the nucleation of clusters occurs at the areas with highly-density dispersed single atoms. Meanwhile, two small clusters of $D-IrCo_{4.9}/NC$ gradually approach closer and finally coalesce into one larger nanoparticle under continuous beam irradiation, as observed in Figure 2I–L, suggesting Ostwald ripening.[43] Our in situ STEM observations vividly reveal the high mobility of single atoms and the formation history of IrCo alloy catalysts.

To elaborate on the role of vacancies in boosting the intrinsic activity, HER is chosen as a model reaction. The electrochemical experiments are conducted in an H-type electrolytic cell with three electrodes by applying CHI 760E workstation. The electrocatalytic performances of $D-IrCo_{4.9}/NC$ and other control samples for HER are assessed in H_2-saturated 0.5 M H_2SO_4 solution. To optimize the catalytic activity of D-IrCo/NC for HER, the catalysts with different Ir/Co mass ratios are synthesized. Among them, $D-IrCo_{4.9}/NC$ exhibits the best activity, as shown in Figure 3A. As observed in Figure 3B,C, $IrCo_{4.9}/NC$ demonstrates the best catalytic activity among four catalysts and only requires an overpotential of 14 mV to deliver a current density of 10 mA cm^{-2}, which is comparable or superior to the behaviors of other Ir-based even Pt-based catalysts, such as $IrCo@NC-850$,[44] $Ni/np-Ir$,[23] $Ir_1@Co/NC$,[45] $Pt_3Co@NCNT$,[44] etc. (Table S5). Ir_1Co_1/NC composed of Ir and Co single atoms, displays poor activity toward HER due to the partial loss of metallic characteristics and strong adsorption of nitrogen on hydrogen in Figure S10. As depicted in Figure 3B, Co/NC shows negligible HER activity relative to $D-IrCo_5/NC$, revealing that metallic Ir in $D-IrCo_{4.9}/NC$ is the actual active site for HER in acid media. Furthermore, the HER activity of $D-IrCo_{4.9}/NC$ remarkably outperforms Ir/NC, suggesting the positive effect of the introduction of Co atoms. To accurately compare the catalytic ability, the activity is normalized based on the mass of Ir dropped on the glassy carbon electrode as shown in Figure 3C. The mass activity of $D-IrCo_{4.9}/NC$ is 3.6-fold higher than that of $IrCo_{5.2}/NC$ at an overpotential of 20 mV, which indicates the significantly improved HER activity after the generation of more defects.
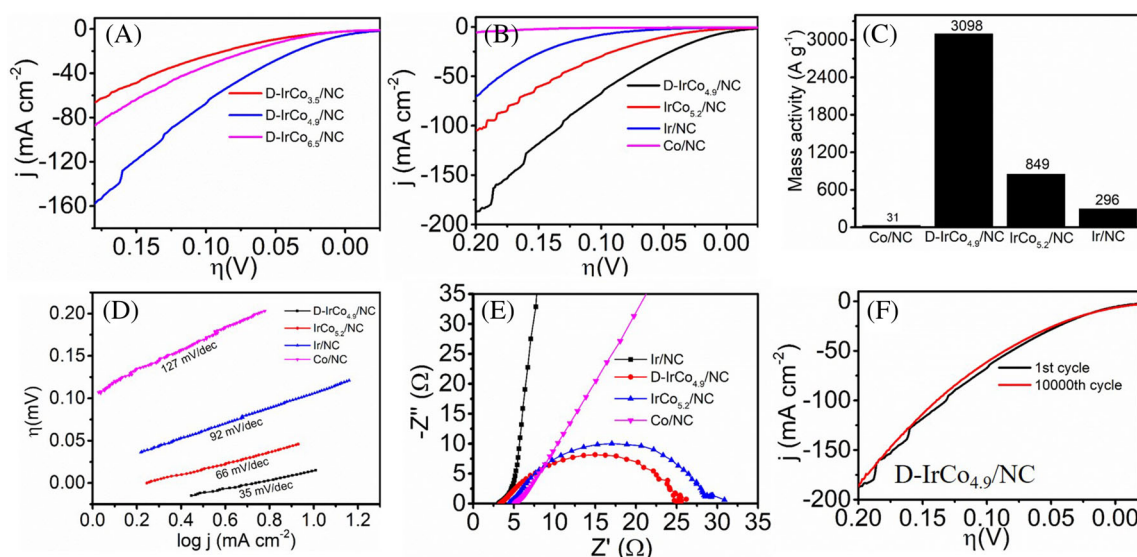
FIGURE 3 Electrocatalytic performance towards HER. (A) The linear scan curves of catalysts with different mass ratios of Ir/Co. (B) HER polarization curves of four catalysts. (C) The mass activities of catalysts at an overpotential of 20 mV. (D) Tafel plots of catalysts. (E) Electrochemical impedance spectroscopy (EIS) of different catalysts. (F) Linear scan curves of D-IrCo$_{4.9}$/NC recorded before and after 10 000 potential cycles

Tafel slope can reflect the reaction kinetics and gain insights into the intrinsic reaction mechanism of HER.[46,47] The Tafel slope of D-IrCo$_{4.9}$/NC is much smaller than that of IrCo$_{4.9}$/NC in Figure 3D, implying the rapid electron transfer. The Tafel slope of 35 mV/dec for D-IrCo$_5$/NC infers that HER follows Volmer–Tafel reaction mechanism and the electrochemical absorption of hydrogen is rate-determining step as shown in Figure S11. However, the Tafel slopes of IrCo$_{4.9}$/NC, Co/NC, and Ir/NC are larger than 40 mV/dec, indicating HER proceed via Volmer–Heyrovsky mechanism. The above Tafel slope results suggest that the introduction of defects changes the pathway of hydrogen evolution and facilitates the electron transfer. Moreover, the electrochemical impedance spectroscopy (EIS) can further manifest the HER kinetics of catalysts at the electrode/electrolyte interface, so the EIS of catalysts is conducted in Figure 3E. The diameter of the semicircle in low-frequency corresponds to charge-transfer resistance (R$_{CT}$).[48] Compared to IrCo$_{4.9}$/NC (25 Ω), the smaller R$_{CT}$ of D-IrCo$_{4.9}$/NC (22 Ω) demonstrates faster charge transfer. Continued cyclic voltammetries (CVs) are operated to evaluate the durability of D-IrCo$_{4.9}$/NC. As observed in Figure 3F, the initial polarization curve is nearly overlapped with the one after 10 000 cycles, unveiling the long-term stability of D-IrCo$_{4.9}$/NC.

Density functional theory (DFT) calculations are carried out to better understand the correlation between structure and activity at the atomic level. The calculation details are presented in the Supporting Information. As

known, hydrogen adsorption Gibbs free energy (ΔG_{H^*}) is deemed a criterion for selecting proper HER electrocatalysts.[49] Therefore, an optimal HER catalyst should have a nearly zero ΔG_{H^*}. Several different theoretical models for IrCo/NC and D-IrCo/NC are constructed. ΔG_{H^*} of the preferable reactive site on bare Ir (111) is −0.24 eV, consisting of the value (−0.32 eV) from the previous study.[50] The structure diagrams of H adsorption on IrCo/NC and D-IrCo/NC with the lowest absolute values of ΔG_{H^*} are shown in Figure 4A,B, respectively. Other structure diagrams are displayed in the Figures S12 and S13. The three-state diagram of HER free-energy process in Figure 4c shows that the optimal ΔG_H on (111) plane of D-IrCo/NC is −0.08 eV, and it is −0.19 eV for IrCo/NC, which indicates the introduction of defects indeed weakens the adsorption of hydrogen and accelerates the hydrogen evolution. Impressively, D-IrCo/NC possesses the lowest absolute value of ΔG_{H^*} when hydrogen situates on the Ir site below the defect compared to that of other sites in Figures 4B and S12. The above result is in accordance with the experimental data and both confirm the crucially positive effect of defects.

To validate the general applicability of this method—generating abundant defects from single-atom dispersed catalyst, transition metal Co is replaced by Fe and IrFe alloy are prepared. As shown in Figure 5A, the peak of (111) plane at 43.57° is located between 44.03° (metallic Fe, [110] plane) and 40.51° (metallic Ir, (111) plane), suggesting the formation of IrFe alloy. Moreover, the lattice spacings of 2.157 and 2.202 Å are ascribed to the (111)

FIGURE 4 The structure diagrams of H adsorption on (A) IrCo/NC and (B) D-IrCo/NC (blue: cobalt; yellow: iridium; pink: hydrogen), (C) Gibbs free-energy profile based on DFT calculations for IrCo/NC and D-IrCo/NC
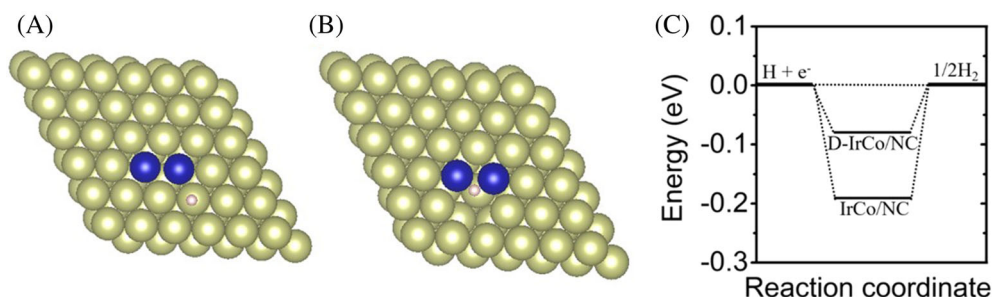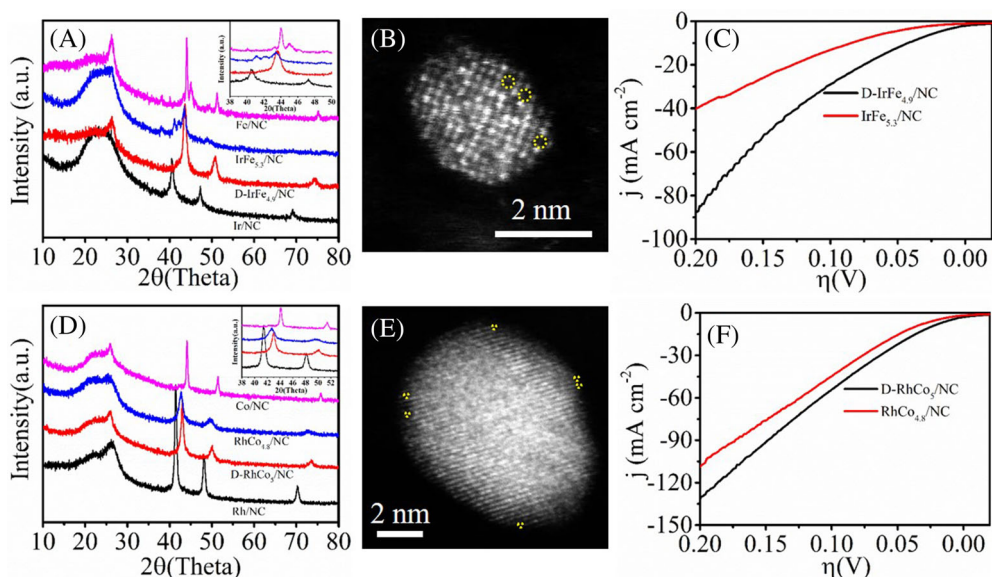

FIGURE 5 (A) and (D) XRD patterns of catalysts, atomic HAADF-STEM images of an individual cluster from (B) D-IrFe$_5$/NC and (E) D-RhCo$_5$/NC, showing the existence of multiple vacancies (marked by yellow circular lines), the polarization curves of (C) IrFe/NC and (F) RhCo/NC

plane of D-IrFe$_{4.9}$/NC. Obviously, there are abundant vacancies in D-IrFe$_{4.9}$/NC in Figure 5B, whereas fewer defects appear in IrFe$_{5.3}$/NC in Figure S14, again indicating more defects form by calcinating single-atom dispersed catalysts. The higher HER activity of D-IrFe$_{4.9}$/NC (η_{10} = 44 mV) than IrFe$_{5.3}$/NC (η_{10} = 87 mV) manifests the promoting effect of defects. Similarly, noble metal Ir is superseded by Rh, and RhCo alloy is synthesized. The corresponding characteristic peaks of D-RhCo$_5$/NC are situated between metallic Rh and Co, confirming the formation of RhCo alloy as observed in Figure 5D. The lattice distance of 2.112 Å is derived from the (111) plane of RhCo alloy in Figure S14c. More defects are observed from D-RhCo$_5$/NC in Figure 5E as compared to RhCo$_{4.8}$/NC in Figure S14d. In Figure 5F, the HER performance of D-RhCo$_5$/NC takes precedence over that of RhCo$_{4.8}$/NC, which verifies the significance of incorporating defects.

4 | CONCLUSION

In summary, a simple and universal strategy to prepare noble-metal alloy catalysts with abundant defects is developed. Upon thermal treatment on the bimetal single-atom dispersed precursors, the resultant D-IrCo$_{4.9}$/NC alloy catalyst with rich defects only requires a low overpotential of 14 mV to achieve the current density of 10 mA/cm^2. In addition, D-IrCo$_{4.9}$/NC also demonstrates a lower Tafel slope and smaller charge transfer resistance compared to IrCo$_{5.2}$/NC with fewer defects. DFT calculation indicates that the introduction of defects can decrease the adsorption of hydrogen and thus accelerate the generation of hydrogen. This method is universal for fabricating other noble-metal alloy catalysts with rich defects, delivering the great potential for various energy applications.

CONFLICT OF INTEREST

The authors declare no conflict of interest.

ORCID

Jiong Zhao 🔗 https://orcid.org/0000-0002-7411-0734

REFERENCES

1. Yao Y, Hu S, Chen W, et al. Engineering the electronic structure of single atom Ru sites via compressive strain boosts acidic water oxidation electrocatalysis. *Nat Catal*. 2019;2(4):304-313. doi:10.1038/s41929-019-0246-2

2. Liu X, Xi S, Kim H, et al. Restructuring highly electron-deficient metal-metal oxides for boosting stability in acidic oxygen evolution reaction. *Nat Commun*. 2021;12(1):5676. doi:10.1038/s41467-021-26025-0

3. Cai R, Jin H, Yang D, et al. Generalized preparation of au NP @ Ni(OH)$_2$ yolk-shell NPs and their enhanced catalytic activity. *Nano Energy*. 2020;71:104542.

4. Huang B, Zhao Y. Iridium-based electrocatalysts toward sustainable energy conversion. *EcoMat*. 2022;4(2):e12176.

5. Tiwari JN, Sultan S, Myung CW, et al. Multicomponent electrocatalyst with ultralow Pt loading and high hydrogen evolution activity. *Nat Energy*. 2018;3(9):773-782. doi:10.1038/s41560-018-0209-x

6. Jin H, Sultan S, Ha M, Tiwari JN, Kim MG, Kim KS. Simple and scalable mechanochemical synthesis of noble metal catalysts with single atoms toward highly efficient hydrogen evolution. *Adv Funct Mater*. 2020;30(25):2000531. doi:10.1002/adfm.202000531

7. Tiwari JN, Dang NK, Sultan S, Thangavel P, Jeong HY, Kim KS. Multi-heteroatom-doped carbon from waste-yeast biomass for sustained water splitting. *Nat Sustain*. 2020;3(7):556-563. doi:10.1038/s41893-020-0509-6

8. Sultan S, Diorizky MH, Ha M, et al. Modulation of cu and Rh single-atoms and nanoparticles for high-performance hydrogen evolution activity in acidic media. *J Mater Chem A*. 2021;9(16):10326-10334. doi:10.1039/D1TA01067K

9. Zhang SL, Lu XF, Wu ZP, Luan D, Lou XW(D). Engineering platinum-cobalt nano-alloys in porous nitrogen-doped carbon nanotubes for highly efficient electrocatalytic hydrogen evolution. *Angew Chem Int Ed*. 2021;60(35):19068-19073. doi:10.1002/anie.202106547

10. Zheng X, Qin M, Ma S, et al. Strong oxide-support interaction over IrO$_2$/V$_2$O$_5$ for efficient pH-universal water splitting. *Adv Sci*. 2022;9(11):2104636.

11. Chen K, Wang Z, Wang L, et al. Boron nanosheet-supported Rh catalysts for hydrogen evolution: a new territory for the strong metal-support interaction effect. *Nano-Micro Lett*. 2021;13(1):138. doi:10.1007/s40820-021-00662-y

12. Deng L, Hu F, Ma M, et al. Electronic modulation caused by interfacial Ni−O−M (M = Ru, Ir, Pd) bonding for accelerating hydrogen evolution kinetics. *Angew Chem Int Ed*. 2021;60(41):22276-22282. doi:10.1002/anie.202110374

13. Zhu J, Huang Y, Mei W, et al. Effects of intrinsic pentagon defects on electrochemical reactivity of carbon nanomaterials. *Angew Chem Int Ed*. 2019;58(12):3859-3864. doi:10.1002/anie.201813805

14. Lyu P, Nachtigall P. Systematic computational investigation of an Ni$_3$Fe catalyst for the OER. *Catal Today*. 2020;345:220-226. doi:10.1016/j.cattod.2019.09.049

15. Fu Y, Shan Y, Zhou G, et al. Electric strain in dual metal janus nanosheets induces structural phase transition for efficient hydrogen evolution. *Joule*. 2019;3(12):2955-2967. doi:10.1016/j.joule.2019.09.006

16. Li X, Li T, Ma Y, et al. Boosted electrocatalytic N$_2$ reduction to NH$_3$ by defect-rich MoS$_2$ nanoflower. *Adv Energy Mater*. 2018;8(30):1801357. doi:10.1002/aenm.201801357

17. Wang P, Luo Y, Zhang G, et al. Interface engineering of Ni$_x$S$_y$@MnO$_x$H$_y$ nanorods to efficiently enhance overall-water-splitting activity and stability. *Nano-Micro Lett*. 2022;14(1):120. doi:10.1007/s40820-022-00860-2

18. Dang NK, Umer M, Thangavel P, et al. Surface enrichment of iridium on IrCo alloys for boosting hydrogen production. *J Mater Chem A*. 2021;9(31):16898-16905. doi:10.1039/D1TA02597J

19. Song M, Zhou G, Lu N, et al. Oriented attachment induces five-fold twins by forming and decomposing high-energy grain boundaries. *Science*. 2020;367(6473):40-45. doi:10.1126/science.aax6511

20. Flores Espinosa MM, Cheng T, Xu M, et al. Compressed intermetallic PdCu for enhanced electrocatalysis. *ACS Energy Lett*. 2020;5(12):3672-3680. doi:10.1021/acsenergylett.0c01959

21. Dang R, Jia X, Liu X, et al. Controlled synthesis of hierarchical cu nanosheets @ CuO nanorods as high-performance anode material for lithium-ion batteries. *Nano Energy*. 2017;33:427-435. doi:10.1016/j.nanoen.2017.01.024

22. Li S, Li M, Ni Y. Grass-like Ni/cu nanosheet arrays grown on copper foam as efficient and non-precious catalyst for hydrogen evolution reaction. *Appl Catal B*. 2020;268:118392.

23. Yu Y, Jiang K, Luo M, et al. Self-activated catalytic sites on nanoporous dilute alloy for high-efficiency electrochemical hydrogen evolution. *ACS Nano*. 2021;15(3):5333-5340. doi:10.1021/acsnano.0c10885

24. Liu S, Hu Z, Wu Y, et al. Dislocation-strained IrNi alloy nanoparticles driven by thermal shock for the hydrogen evolution reaction. *Adv Mater*. 2020;32(48):2006034. doi:10.1002/adma.202006034

25. Zhang C, Dai L. Targeted defect synthesis for improved electrocatalytic performance. *Chem*. 2020;6(8):1849-1851. doi:10.1016/j.chempr.2020.07.018

26. Qu Y, Chen B, Li Z, et al. Thermal emitting strategy to synthesize atomically dispersed Pt metal sites from bulk Pt metal. *J Am Chem Soc*. 2019;141(11):4505-4509. doi:10.1021/jacs.8b09834

27. Chang J, Wang G, Wang M, et al. Improving Pd−N−C fuel cell electrocatalysts through fluorination-driven rearrangements of

local coordination environment. *Nat Energy.* 2021;6(12):1144-1153. doi:10.1038/s41560-021-00940-4

28. Cai C, Han S, Wang Q, Gu M. Direct observation of yolk–shell transforming to gold single atoms and clusters with superior oxygen evolution reaction efficiency. *ACS Nano.* 2019;13(8):8865-8871. doi:10.1021/acsnano.9b02135

29. Zhou R, Fan X, Ke X, et al. Two-dimensional palladium–copper alloy nanodendrites for highly stable and selective electrochemical formate production. *Nano Lett.* 2021;21(9):4092-4098. doi:10.1021/acs.nanolett.1c01113

30. Zhong M, Tran K, Min Y, et al. Accelerated discovery of CO_2 electrocatalysts using active machine learning. *Nature.* 2020;581(7807):178-183. doi:10.1038/s41586-020-2242-8

31. Tiwari JN, Harzandi AM, Ha M, et al. High-performance hydrogen evolution by Ru single atoms and nitrided-Ru nanoparticles implanted on N-doped graphitic sheet. *Adv Energy Mater.* 2019;9(26):1900931. doi:10.1002/aenm.201900931

32. Lu B, Guo L, Wu F, et al. Ruthenium atomically dispersed in carbon outperforms platinum toward hydrogen evolution in alkaline media. *Nat Commun.* 2019;10(1):631. doi:10.1038/s41467-019-08419-3

33. Kresse G, Furthmüller J. Efficient iterative schemes for ab initio total-energy calculations using a plane-wave basis set. *Phys Rev B.* 1996;54(16):11169-11186. doi:10.1103/PhysRevB.54.11169

34. Kresse G, Furthmüller J. Efficiency of ab-initio total energy calculations for metals and semiconductors using a plane-wave basis set. *Comput Mater Sci.* 1996;6(1):15-50. doi:10.1016/0927-0256(96)00008-0

35. Blöchl PE. Projector augmented-wave method. *Phys Rev B.* 1994;50(24):17953-17979. doi:10.1103/PhysRevB.50.17953

36. Perdew JP, Burke K, Ernzerhof M. Generalized gradient approximation made simple. *Phys Rev Lett.* 1996;77(18):3865-3868. doi:10.1103/PhysRevLett.77.3865

37. Perdew JP, Ernzerhof M, Burke K. Rationale for mixing exact exchange with density functional approximations. *J Chem Phys.* 1996;105(22):9982-9985. doi:10.1063/1.472933

38. Grimme S, Antony J, Ehrlich S, Krieg H. A consistent and accurate ab initio parametrization of density functional dispersion correction (DFT-D) for the 94 elements H-Pu. *J Chem Phys.* 2010;132(15):154104. doi:10.1063/1.3382344

39. Pack JD, Monkhorst HJ. "Special points for Brillouin-zone integrations"—a reply. *Phys Rev B.* 1977;16(4):1748-1749. doi:10.1103/PhysRevB.16.1748

40. Nørskov JK, Bligaard T, Logadottir A, et al. Trends in the exchange current for hydrogen evolution. *J Electrochem Soc.* 2005;152(3):J23. doi:10.1149/1.1856988

41. Huang L, Zheng F, Deng Q, et al. In situ scanning transmission electron microscopy observations of fracture at the atomic scale. *Phys Rev Lett.* 2020;125(24):246102. doi:10.1103/PhysRevLett.125.246102

42. Zhang X, Zhang M, Deng Y, et al. A stable low-temperature H_2-production catalyst by crowding Pt on α-MoC. *Nature.* 2021;589(7842):396-401. doi:10.1038/s41586-020-03130-6

43. Moliner M, Gabay JE, Kliewer CE, et al. Reversible transformation of Pt nanoparticles into single atoms inside high-silica chabazite zeolite. *J Am Chem Soc.* 2016;138(48):15743-15750. doi:10.1021/jacs.6b10169

44. Zhou YQ, Zhang LF, Suo HL, et al. Atomic cobalt vacancy-cluster enabling optimized electronic structure for efficient water splitting. *Adv Funct Mater.* 2021;31(26):2101797. doi:10.1002/adfm.202101797

45. Lai W-H, Zhang L-F, Hua W-B, et al. General π-electron-assisted strategy for Ir, Pt, Ru, Pd, Fe, Ni single-atom electrocatalysts with bifunctional active sites for highly efficient water splitting. *Angew Chem Int Ed.* 2019;58(34):11868-11873. doi:10.1002/anie.201904614

46. Xu J, Liu T, Li J, et al. Boosting the hydrogen evolution performance of ruthenium clusters through synergistic coupling with cobalt phosphide. *Energy Environ Sci.* 2018;11(7):1819-1827. doi:10.1039/C7EE03603E

47. Wu D, Wei Y, Ren X, et al. $Co(OH)_2$ nanoparticle-encapsulating conductive nanowires array: room-temperature electrochemical preparation for high-performance water oxidation electrocatalysis. *Adv Mater.* 2018;30(9):1705366. doi:10.1002/adma.201705366

48. Thalluri SM, Bai L, Lv C, Huang Z, Hu X, Liu L. Strategies for semiconductor/electrocatalyst coupling toward solar-driven water splitting. *Adv Sci.* 2020;7(6):1902102. doi:10.1002/advs.201902102

49. Chen D, Pu Z, Wang P, et al. Mapping hydrogen evolution activity trends of intermetallic Pt-group silicides. *ACS Catal.* 2022;12(4):2623-2631. doi:10.1021/acscatal.1c05175

50. Peng Y, Liu Q, Lu B, et al. Organically capped iridium nanoparticles as high-performance bifunctional electrocatalysts for full water splitting in both acidic and alkaline media: impacts of metal–ligand interfacial interactions. *ACS Catal.* 2021;11(3):1179-1188. doi:10.1021/acscatal.0c03747

SUPPORTING INFORMATION

Additional supporting information can be found online in the Supporting Information section at the end of this article.